Mn_2TeO_6: Complex antiferromagnetism as a consequence of the Jahn-Teller distortion

N. Matsubara,[1,2] C. Martin,[1,*] B. Vertruyen,[3] A. Maignan,[1] F. Fauth,[4] P. Manuel,[5] V. Hardy,[1]
D. Khalyavin,[5] E. Elkaïm,[6] and F. Damay[2]

[1]*CRISMAT, 6 bvd Maréchal Juin, 14050 Caen Cedex, France*
[2]*Laboratoire Léon Brillouin, CEA-CNRS UMR12, Université Paris-Saclay, 91191 Gif-sur-Yvette Cedex, France*
[3]*GREENMAT, CESAM Research Unit, Université de Liège, Institut de Chimie B6, 13 Allée du 6 août, 4000 Liège, Belgium*
[4]*CELLS ALBA Synchrotron, E-08290 Barcelona, Spain*
[5]*ISIS Facility, Rutherford Appleton Laboratory-CCLRC, Chilton, Didcot, Oxfordshire OX11 0QX, United Kingdom*
[6]*Synchrotron Soleil, Saint-Aubin BP 48, 91192 Gif-sur-Yvette Cedex, France*

(Received 27 November 2018; revised manuscript received 27 May 2019; published 8 July 2019)

Structural and magnetic transitions in the distorted inverse trirutile Mn_2TeO_6 have been studied between 1.5 and 300 K using magnetization, dielectric permittivity, and specific heat measurements combined with synchrotron x-ray- and neutron-diffraction techniques on polycrystalline samples. A first-order structural transition, strongly hysteretic, occurs progressively over a large temperature span and is characterized by a broad maximum peaking at 53 K in the specific heat data. This structural transition is followed by two antiferromagnetic transitions, to commensurate and incommensurate magnetic orders, at 48 and 26 K, respectively. This succession of structural and magnetic transitions is interpreted as originating from a delicate balance between Jahn-Teller distortion of MnO_6 octahedra, rigid TeO_6 units, and their consequences on orbital and spin orderings.

DOI: 10.1103/PhysRevB.100.014409

I. INTRODUCTION

The family of inverse trirutiles known since 1960 [1] has been the subject of recent interest in the search for multiferroic materials, as illustrated by the reports on the magnetoelectric properties of Cr_2WO_6 and Fe_2TeO_6 [2–6]. In that respect, much less is known concerning the crystal structure and magnetic properties of Mn_2TeO_6 [7,8]. Some of us recently reported [9] that this compound exhibits a structural transition at 673 K, from a high-temperature tetragonal (HTT) $P4_2/mnm$ structure to a room-temperature monoclinic (RTM) $P2_1/c$ larger cell. This RTM monoclinic phase is characterized by pairs of compressed and elongated MnO_6 octahedra, sandwiched between rigid TeO_6 within the -(Mn-Mn-Te)$_\infty$- infinite chains running along the a_{RTM} axis (Fig. 1) [9]. Some disorder related to Mn/Te site intermixing was observed and found to decrease with improved crystallinity [9], explaining why previous studies reported two possible space groups at room temperature [7,8]. The neutron-diffraction study in Ref. [8] was carried out on the Mn_2TeO_6 form reported as tetragonal and evidenced a noncollinear commensurate magnetic ordering below 25.5 K ($\mathbf{k} = 0\,0\,1/2$), very different from the G-type ($\mathbf{k} = 0\,0\,0$) order of Cr_2TeO_6 or Fe_2TeO_6 [10–12].

We report here an investigation of polycrystalline Mn_2TeO_6 samples, prepared using different heat treatments. Susceptibility and specific heat measurements between 5 and 300 K evidence a very complex behavior, involving six transitions below 55 K. The isothermal magnetic-field dependence of the magnetization reveals a metamagnetic transition at low temperature and a stable antiferromagnetic state up to the maximal field of 14 T around 40 K. Synchrotron x-ray- and neutron-powder-diffraction experiments are used to study the crystalline and magnetic structures versus temperature, showing an unusually complex structural and magnetic behavior.

II. EXPERIMENTAL

A. Synthesis

Mn_2TeO_6 was prepared by solid-state reaction using manganese oxalate ($MnC_2O_4 \cdot 2H_2O$) and commercial telluric acid (H_6TeO_6, Fluka, >99%) [9]. These precursors were weighted in the Mn/Te = 2 ratio and mixed in an agate mortar before being calcined in an alumina crucible at 550 °C for 12 h in air. The powder was then ground again, pressed in the shape of bars ($\cong 2 \times 2 \times 12\,mm^3$) or pellets (1-cm diameter) and sintered at 600 °C for 24 h in air. Then several annealings were performed, increasing progressively the temperature up to 700 °C in O_2 flow (to avoid Te losses) and the time of annealing up to 2 wk. The quality of the samples, which were also observed by scanning electron microscopy (FEI XL30 FEG-SEM), was checked by x-ray diffraction at room temperature (RT). All the patterns are characteristic of the inverse trirutile structure and the broadening of the Bragg peaks correlates well with the heat-treatment conditions. As previously reported [9], disorder in the distribution of Mn and Te on the cationic sites depends on the temperature and duration of the oxygen annealing.

B. Magnetic characterizations

Magnetic measurements versus temperature were performed with a Quantum Design 5T superconducting quantum

*christine.martin@ensicaen.fr

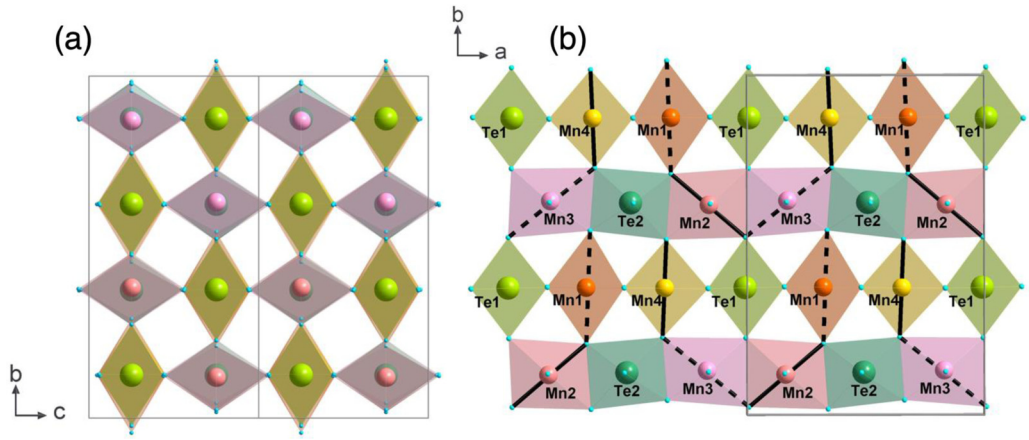

FIG. 1. Room-temperature monoclinic structure of Mn_2TeO_6 ($P2_1/c$ space group with $a = 9.103$ Å, $b = 13.046$ Å, $c = 6.466$ Å, and $\beta = 90.03°$) [9] projected along a (a) and c (b). Elongated and compressed MnO_6 octahedra are highlighted by dashed and full black lines corresponding to long and short Mn-O distances, respectively. Two types of -(Mn-Mn-Te)$_\infty$- chains run along a, MnO_6, and TeO_6 octahedra are in pink/orange/yellow/purple, and dark/light green, respectively.

interference device magnetometer in zero-field-cooled warming (*zfcw*) or field-cooled warming (*fcw*) or field-cooled cooling (*fcc*) modes between 5 and 300 K. The magnetic susceptibility is obtained by taking $\chi = M/H$, where M is the magnetization obtained by dividing the measured magnetic moment by the sample mass and H is the external applied magnetic field (in Oe). ac magnetic susceptibility curves were recorded by using the magnetic option of a Quantum Design 9T physical property measurement system (PPMS) with $h_{dc} = 0$ T, $h_{ac} = 0.001$ T, and $f = 100$ Hz, 1 kHz, and 10 kHz. Isothermal $M(H)$ curves were also collected using the AC measurement system (ACMS) option of the PPMS for magnetic fields up to 14 T.

C. Dielectric measurements

Dielectric measurements were carried out with an Agilent 4284 LCR meter by using a home-made sample holder set in the PPMS. Platelets of $2 \times 2 \times 0.5\,mm^3$ were cut in the bars or pellets of Mn_2TeO_6. Silver paste electrodes were deposited on the largest parallel surfaces. The dielectric permittivity (ε') versus temperature was measured between 8 and 200 K, while warming or cooling, at different frequencies ($f = 5$–100 kHz), with an excitation voltage amplitude of 1 V. Isothermal $\varepsilon'(H)$ curves were collected by varying the applied magnetic field between 0 and 14 T.

D. Specific heat

Heat-capacity measurements were carried out by means of an experimental setup developed by Quantum Design for the PPMS, which is based on a semiadiabatic relaxation technique. Each measurement relies on a temperature pulse (of magnitude ΔT_{pulse}) caused by a transient heating power applied to the platform hosting the sample; the platform temperature is recorded versus time during the heating branch of the process (with power on) and during the cooling branch (when the power is off). The heat capacity is derived from the analysis of this thermal response. In this standard approach (hereafter referred to as the QD method), the heat capacity is derived from an overall fitting of both the heating and cooling branches, within the framework of a 2-τ model. A second approach, related to previous works [13,14], is based on a point-by-point (PBP) analysis of a series of closely spaced pulses. It is a time-resolved method, which allows one to address separately the heating and cooling branches within a 1-τ approximation. Provided there is a good thermal contact of the sample onto the platform, the small error induced by the use of a 1-τ approximation can safely be corrected by scaling onto results of the QD data (2-τ) recorded outside the transitions. The main interest of the PBP method is that it makes possible the investigation of sharp and hysteretic first-order transitions, contrary to the standard QD method. However, in case of very wide hysteresis ($> \Delta T_{pulse}$), the analysis becomes limited to the heating branch only. An additional advantage of the PBP method is the possibility to reach high-resolution in temperature. For the QD method, we used a data spacing of 0.5 K with $\Delta T_{pulse} = T/100$. For the PBP technique, 50 heat pulses were recorded in the range 15–65 K (i.e., starting temperatures spaced by 1 K), using $\Delta T_{pulse} = 6$ K and keeping only the central part of each pulse for the analysis yields $C(T)$ segments over $\approx$2 K with a resolution of $\approx$0.05 K; doing so allows one to cover the 15–65 K range with an overlapping of $\approx$1 K between successive $C(T)$ segments. Each of these pulses was preceded by a warming up to 100 K followed by a cooling down to 15 K, in order to discard any history effects related to hysteretic transitions.

E. Synchrotron x-ray diffraction

Synchrotron x-ray-powder-diffraction (SXRPD) experiments were performed on the BL04-MSPD beamline of the ALBA synchrotron [15]. Data were collected between 10 and 295 K, using as detection setup both the high angular resolution mode (multianalyzer crystal MAD) and the high-intensity mode (position-sensitive detector MYTHEN), at wavelength $\lambda = 0.4142$ Å, with the sample enclosed in a glass capillary (0.5-mm inner diameter, spinning to improve powder averaging) within the so-called Dynaflow He flow cryostat

[16]. Several experimental conditions were used, such as a stable temperature or sweeping mode (rate 1 K min^{-1}), while warming or cooling.

F. Neutron diffraction

Neutron-powder diffraction (NPD) versus temperature was performed on the G4.1 diffractometer ($\lambda = 2.426$ Å) from 1.5 to 300 K (at LLB-Orphée) and on the WISH high-resolution time-of-flight diffractometer (ISIS Facility), in the same temperature range. Data were recorded while warming in both experiments. Symmetry analysis and Rietveld refinements were performed with tools from the FULLPROF suite [17] and the Bilbao Crystallographic server [18].

III. RESULTS

A. Preliminary study

The effect of different heat treatments upon the $\chi(T)$ curves of Mn_2TeO_6 is shown in Fig. 2(a). For all samples, with increasing temperature, the magnetic signal increases slightly up to a first characteristic temperature ≈27 K, corresponding to a susceptibility maximum. The samples prepared at 600 °C in air exhibit distinctly this transition only, close to the T_N value of 25.5 K reported previously for a Mn_2TeO_6 sample prepared in similar conditions [8]. For the annealed compounds, further increasing the temperature above 27 K, a second peak is observed on the $\chi(T)$ curves at a temperature which, in contrast with the first one, varies slightly from sample to sample in the range ≈55–65 K. With annealing, the cationic order increases [9], the transition temperature decreases, and the intensity of the magnetic signal increases, leading to a better-defined peak. It appears not to be possible to lower this transition temperature below ≈55 K. Annealing does not affect the lattice parameters which stay very similar, with a cell volume evolution <0.5%. Differences between samples are mostly larger grains [illustrated in SEM images of Figs. 2(c) and 2(d)] and narrower Bragg peaks [in SXRPD patterns of Fig. 2(b)] for the annealed sample (700 °C in O_2) compared to the as-prepared one (600 °C in air).

The inverse of the susceptibility curves shows a large linear domain, for which Curie-Weiss fitting leads to similar μ_{eff} values ≈5.0 μ_B/Mn, confirming the trivalent state of manganese (as the Mn^{3+} expected theoretical value is 4.90 μ_B) [8,9]. The departure from linearity of the $1/\chi(T)$ curves occurs at higher temperature for the as-prepared sample (≈130 K instead of 110 K) and the value of $|\theta_P|$ is also larger for the latter ($\theta_P \approx -69$ K against −42 K after annealing). For all the samples, the 0.01-T *zfcw* and *fcw* $\chi(T)$ curves are nearly superimposed (not shown), confirming the strong antiferromagnetic character of Mn_2TeO_6.

B. Magnetic and dielectric properties

In the further magnetic and dielectric experiments described below, only the Mn_2TeO_6 sample annealed in oxygen at 700 °C for the longest duration is considered, to ensure better crystallinity, higher cationic order, and better sintering for electrical measurements. The comparison of the $\chi(T)$ curves collected in 0.01 T on cooling (*fcc*) and warming (*fcw*)

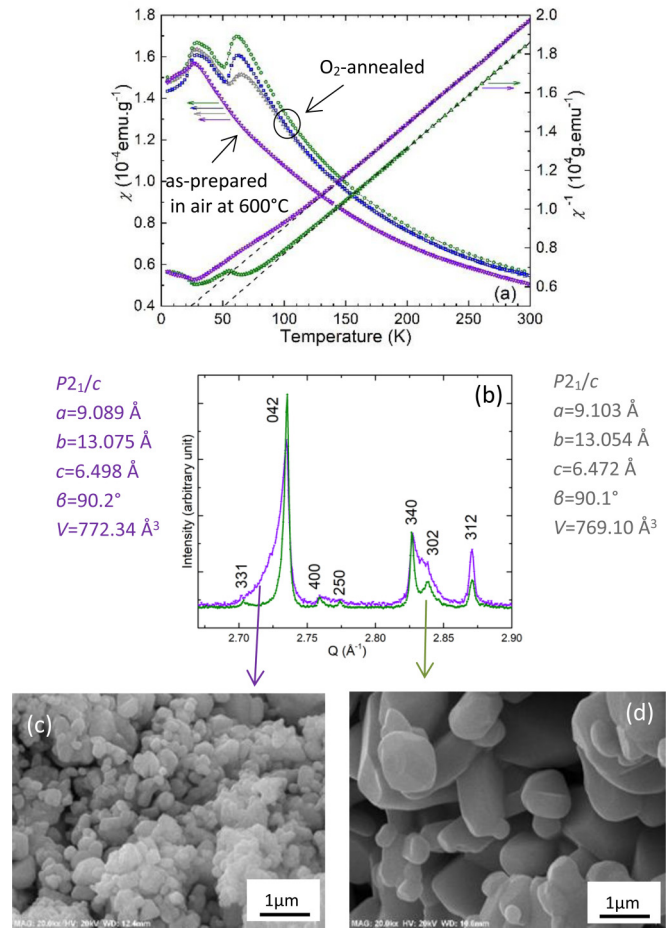

FIG. 2. (a) Magnetic susceptibility curves of several Mn_2TeO_6 samples (as-prepared sample in dark pink and O_2-annealed samples from gray to green with increasing time of the plateau at 700 °C) recorded in zero-field-cooled warming, 0.01 T [$\chi(T)$, left *y* axis] and associated inverse curves with Curie-Weiss fitting (dotted lines) [$1/\chi(T)$, right *y* axis]. (b) SXRPD patterns (in a small selected 2θ range) of as-prepared and annealed samples, indexation corresponding to the space group and lattice parameters given on each side. (c), (d) Corresponding SEM images.

confirms that the two transitions described above exist for both modes [curves 2-*fcc* and 3-*fcw* in Fig. 3(a)]. In addition, a spectacular temperature hysteresis of ≈10 K is observed for the high-temperature transition, with a maximum of the curve at ≈48 K in cooling mode and ≈57 K in warming. The magnetic transition is also well evidenced in the $[d\chi/dT](T)$ curves [curves *d2* and *d3* in Fig. 3(a)], at ≈43 and 53 K in *fcc* and *fcw* modes, respectively. The 10 K hysteresis remains unchanged when a magnetic field is applied (from 0.01 to 5 T), as the characteristic temperatures in cooling and warming do not depend on the magnetic field [Fig. 3(b)]. These observations suggest that a structural transition occurs in this temperature range, that will be discussed in the light of the synchrotron- and neutron-diffraction results in Secs. III D and III E.

In the $\chi(T)$ curves, the low-temperature transition corresponds to a broad local maximum with a slight shoulder on the low-temperature side, revealed as a second peak in the

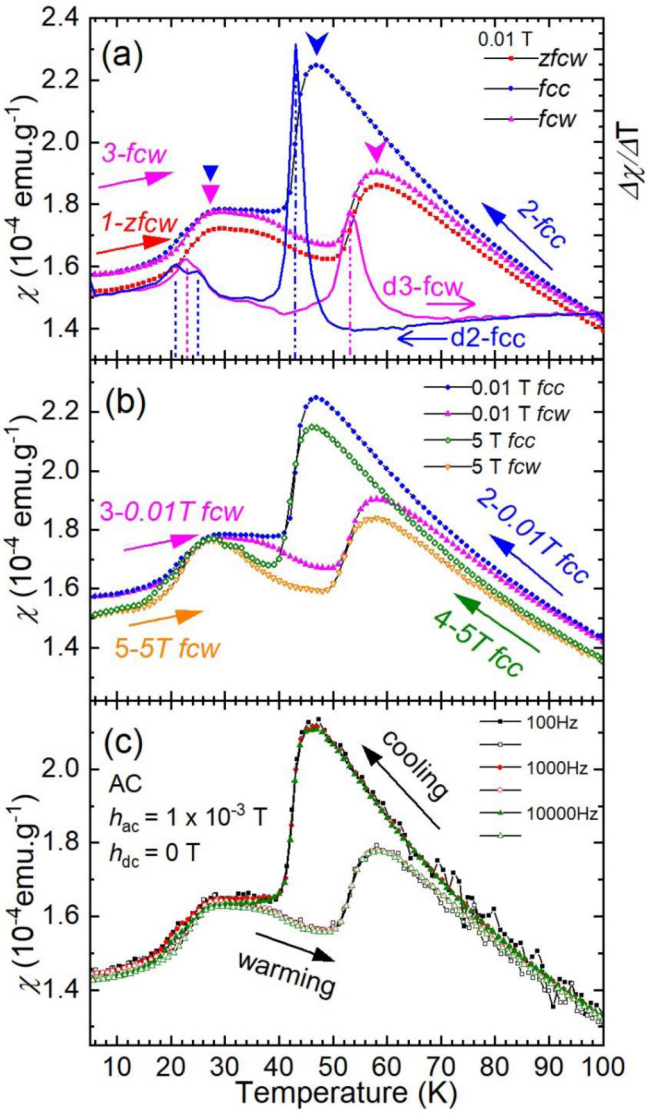

FIG. 3. (a) $Mn_2TeO_6\chi(T)$ curves recorded in 1-z*fcw*, 2-*fcc,* and 3-*fcw* modes (left *y* axis), and corresponding *T* derivative (d2-*fcc* and d3-*fcw*) curves (right *y* axis). (b) Comparison of the $\chi(T)$ curves measured in 0.01 T—like in panel (a)—with the curves measured in 5 T (4-*fcc* and 5-*fcw*). (c) ac susceptibility curves while cooling or warming measured at three frequencies between 10^2 and 10^4 Hz.

$[d\chi/dT](T)$ curves. The transition at ≈25 K does not vary with the mode (*fcw* and *fcc*). The second peak is affected by a small hysteresis with values of ≈21 and 23 K for the *fcc* and *fcw* modes, respectively. The derivative curves also suggest an additional transition around ≈35 K, which seems to be magnetic-field sensitive [Fig. 3(b)]. This complex sequence of transitions motivates the C_p, synchrotron, and NPD studies, reported in Secs. III C–E.

The temperature dependence of the dielectric permittivity (Fig. 4) shows a change of slope (better seen around 43 K in the cooling data), although pyroelectric measurements do not reveal any electrical polarization below that temperature. The location of the change of slope and the fact that $\varepsilon'(T)$ is hysteretic in the same temperature range as $\chi(T)$ underline links between electrical, structural, and magnetic properties.

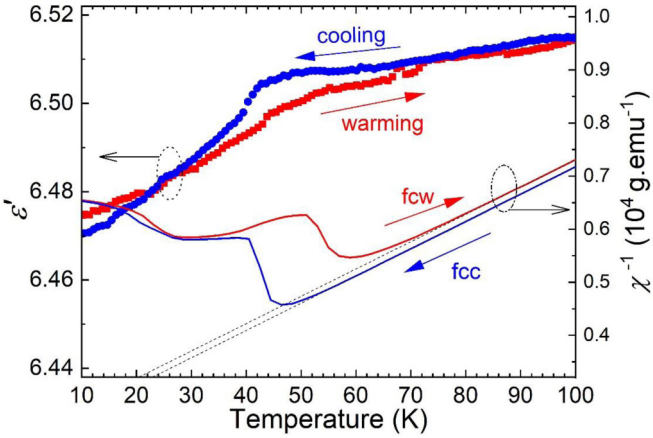

FIG. 4. Dielectric permittivity ε' versus temperature, recorded while cooling or warming between 10 and 100 K, in zero magnetic field (left *y* axis). Inverse of *fcc* and *fcw* magnetic susceptibility measured in 0.01 T, in the same temperature range, with the corresponding Curie-Weiss fitting as dotted lines (right *y* axis).

The absence of frequency dependence on $\chi'(T)$ [Fig. 3(c)] and $\varepsilon'(T)$ (not shown) outlines that electric charges and spins do not exhibit dynamical features, ruling out dipolar glass behavior.

The $M(H)$ curves collected at several temperatures below 60 K are characteristic of a complex magnetic behavior, as shown by the selection presented in Fig. 5. The curves collected at $T \leqslant 10$ K are similar [illustrated by the 5 K curve in Fig. 5(a)]: they first show a linear domain, with similar slopes, then for $\mu_0 H > 4.5$ T they adopt a flattened S shape corresponding to a smooth metamagnetic transition, followed by another linear $M(H)$ regime for $\mu_0 H > 13$ T with a sharper slope. For higher temperatures [like 30, 40, 50, and 60 K in Figs. 5(a) and 5(b)] no such transition is revealed, indicating that the metamagnetic transition exists only for the low-temperature magnetic state below 30 K. This is confirmed

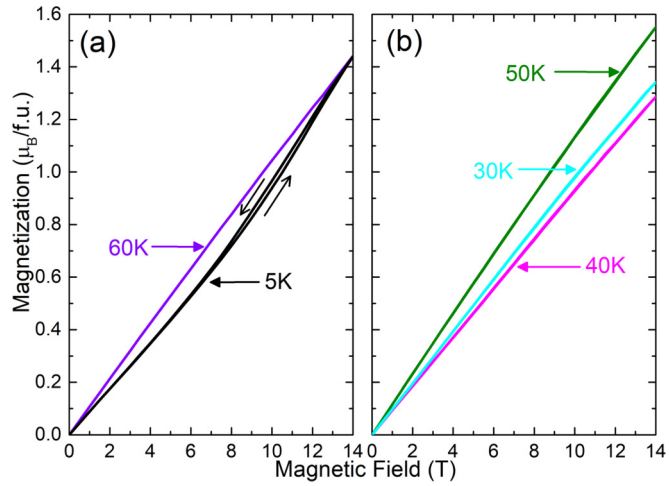

FIG. 5. Isothermal half-loop magnetization curves versus magnetic field, applied from 0 to 14 T then back to 0 T. Curves are split into two panels for clarity: (a) $T = 5$ and 60 K, (b) $T = 30$, 40, and 50 K.

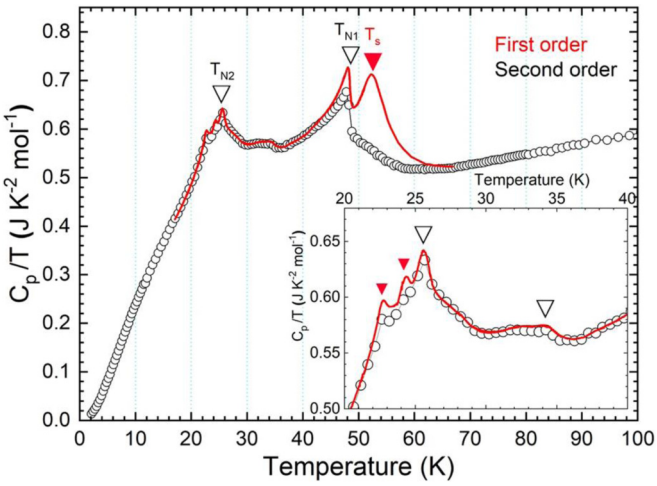

FIG. 6. Temperature evolution of the specific heat C_p/T of Mn_2TeO_6, in QD mode (black symbols) and PBP mode (red line) applied to the heating branches of 50 overlapping pulses (details in the Experimental section). Red and black triangles indicate first- and second-order transitions, respectively. Inset: Zoom in the 20–40 K range.

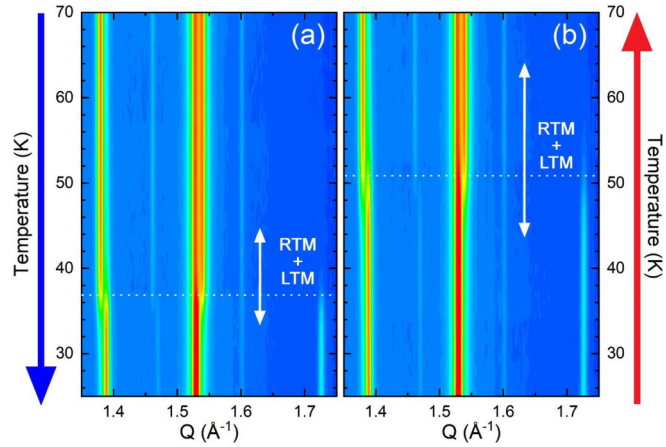

FIG. 7. Synchrotron x-ray data of Mn_2TeO_6 versus temperature: (a) cooling and (b) warming runs, showing the strong hysteresis of the structural transition. Intensities are displayed in logarithmic scale to highlight the weak reflections growing below T_{N2}. The extended temperature range in which the structural transition takes place is highlighted by the white vertical arrows delimiting the coexistence of the two (RTM+LTM) phases (based on a 10% threshold).

by the 20 K curve (not shown), which exhibits an intermediate behavior, suggesting that the metamagnetic transition is associated with the antiferromagnetic (AFM) state below the low-temperature magnetic transition ($T < 25$ K). It exhibits a small hysteresis, as shown for 5 K in Fig. 5(a), which could indicate a structural transition. Moreover, the fact that the magnetization values recorded at 14 T are smaller at 30 and 40 K compared with 5 or 60 K means that application of the magnetic field does not transform the low-temperature state into the magnetic state observed above the low-temperature magnetic transition. All these results suggest therefore that the more stable AFM state is observed between the low and high-temperature magnetic transitions, at ≈40 K.

The effect of magnetic field on the dielectric permittivity is very small (not shown). The $\varepsilon'(H)_{10\,K}$ curve exhibits a slight negative magnetodielectric effect for $\mu_0 H > 5$–6 T, i.e., in the field range corresponding to the metamagnetic transition at 10 K.

C. Specific heat

To go further in the understanding of the susceptibility features, specific heat (C_p) measurements were carried out upon warming (Fig. 6). A complex picture emerges again, with six transitions observed in the range 15–100 K, identified by red and black triangles in Fig. 6. Black arrows correspond to second-order transitions (no latent heat, no hysteresis), as one observes the same signature for both QD and PBP measuring techniques, while red arrows indicate first-order transitions. In the temperature range of the high-temperature hysteretic transition observed on $\chi(T)$ measurements, specific-heat data actually show two adjacent transitions: the pronounced first-order one at $T_S = 53$ K is quite broad and will be shown in the next section to be a structural transition. It is associated with a second-order transition at $T_{N1} = 48$ K. Another second-order transition is seen at $T_{N2} = 26$ K, in good agreement with the nonhysteretic transition observed around 25 K on the $d\chi/dT$ curve. Two additional transitions are observed, corresponding to weak but sharp peaks on the $C/T(T)$ curves below T_{N2}, at 24.5 and 23 K (inset of Fig. 6) and could match the hysteretic transition observed on the $\chi(T)$ derivative around 23 K.

D. Synchrotron x-ray diffraction

To investigate these transitions, a synchrotron x-ray-diffraction study was performed in the 10–200 K range. As illustrated in Fig. 7 and in Fig. 8 with four representative patterns, a structural transition occurs from the room temperature monoclinic (RTM) structure [9] to a low-temperature structure, called thereafter LTM phase (and described later). The two phases coexist over a broad temperature range, shown by the white arrows in Fig. 7. Such a coexistence range is generally expected for a first-order structural transition, although it is quite large in this case, from ≈ 45 to 65 K in warming. This broad temperature range could indeed explain why the first-order transition peaking at $T_S = 53$ K in the C_p data is extremely broad (Fig. 6). The hysteresis observed between the cooling and the warming synchrotron runs [Figs. 7(a) and 7(b)] is in agreement with the χ results showing a ≈ 10 K hysteresis (Fig. 3). No further transitions are observed below T_S on the synchrotron data (Fig. 7) suggesting a magnetic-only origin for T_{N2}.

Le Bail fitting of the data collected during the SXRPD warming run gives the evolution of the cell parameters with temperature (Fig. 9). For convenience, the structural evolution is described from RT to low temperatures. Decreasing temperature, the model remains the RTM inverse trirutile structure of $P2_1/c$ space group [9] and, at the transition, a clear cell contraction takes place in the bc plane [Figs. 9(b) and 9(c)], while the a parameter remains temperature independent [Fig. 9(a)]. The most obvious feature is the enhancement of the monoclinic distortion as the temperature decreases

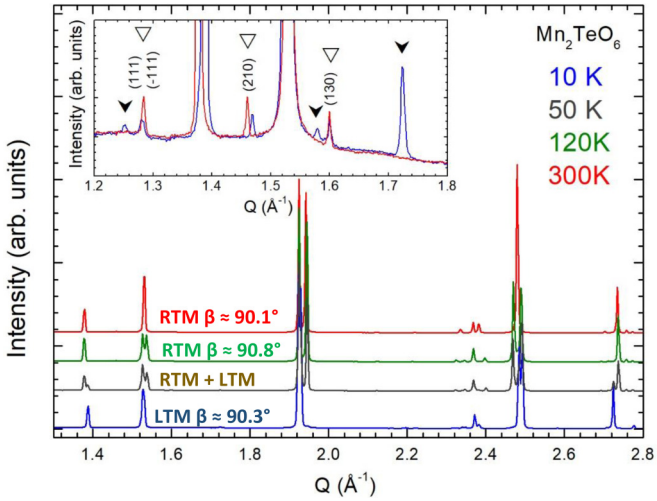

FIG. 8. Synchrotron x-ray data of Mn_2TeO_6 in the 1.2–2.8-$Å^{-1}$ range, at 10 K (blue), 50 K (dark yellow), 120 K (green), and 300 K (red) (data are shifted for clarity). Inset: Zoom-in on the low-intensity area of 10 and 300 K patterns. The small Bragg peaks outlined by empty down triangles result from the doubling along the b axis of the inverse trirutile cell (HTT) and are indexed in the RTM cell. The superstructure Bragg peaks only observed in the LTM phase are shown by small black arrows.

(especially below 200 K), since the β angle increases from 90.03° at RT to 90.74° at 53 K [inset of Fig. 9(a)]. Le Bail fits of the LTM phase (outside the range of phase coexistence, that is, $T < 45$ K) were performed to determine the low-temperature cell parameters and symmetry. Keeping a holohedric monoclinic space group and a RTM-like structure, the main Bragg peaks can be indexed with $a \approx 9.03$ Å, $b \approx 13.05$ Å, and $c \approx 6.50$ Å, with $\beta \approx 90.23°$ at 10 K. This clearly corresponds to a compression of the cell along a, simultaneously with a strong expansion of the b and c parameters, while the monoclinic distortion is strongly reduced (Fig. 9). A small accident can also be observed on the $a(T)$ and $b(T)$ evolutions around T_{N2} and the first-order transitions identified by C_p measurements [Figs. 9(a) and 9(b)]. This effect is only subtle and corresponds roughly to a 0.02% decrease of those cell parameter value, that is, just outside the error values. Magnetoelastic effects at these transitions remain therefore to be confirmed. Although the small peaks characteristic of the superstructure in the RTM cell (i.e., the double-b parameter compared to usual inverse trirutiles) are still clearly observed, several extra peaks remain nonindexed within these Le Bail fittings (inset of Fig. 8, hollow triangles and black arrows, respectively).

Rietveld refinements using the RTM phase structural model were performed following the procedure described in Ref. [9], which decomposes the structure into sets of symmetry-adapted displacement modes specified with respect to the $P4_2/mnm$ space group of the HTT inverse trirutile structure, to follow the evolution with temperature of the distortion primary mode before the structural transition. The reliability of these refinements was impaired by the increasing strain resulting from the monoclinic distortion of the crystal structure [19] and the coexistence of the RTM and LTM phases below 100 K. Nevertheless, they indicate that the

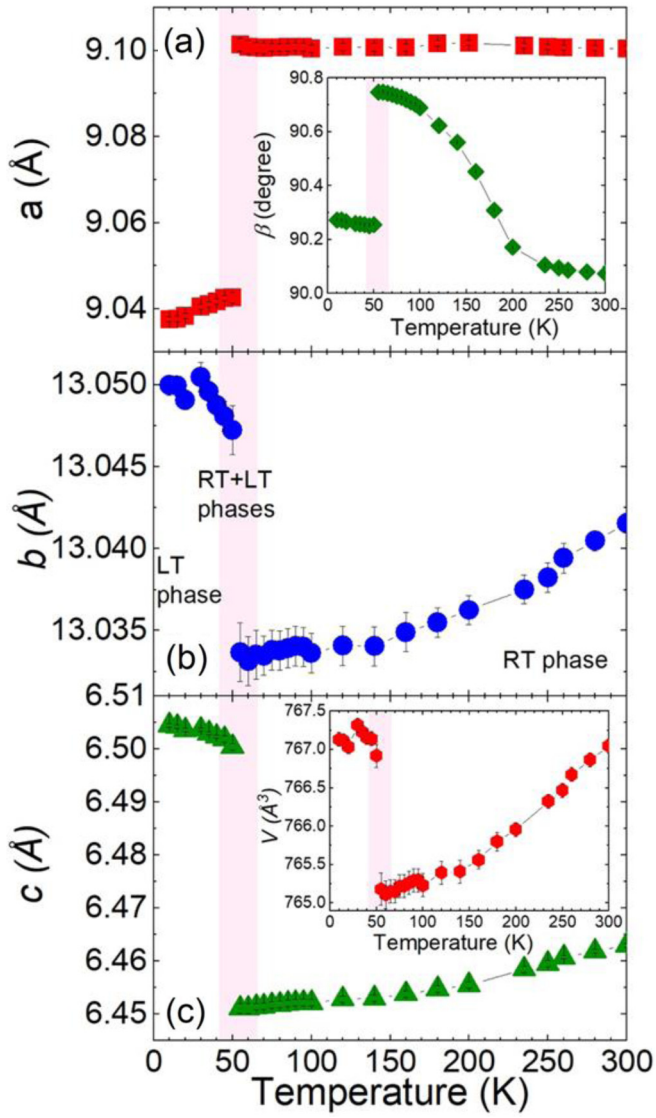

FIG. 9. Temperature evolution of the cell parameters of Mn_2TeO_6 extracted from Le Bail refinements of the synchrotron x-ray data collected during the warming run: (a) cell parameter a and monoclinic angle β, (b) cell parameter b, and (c) cell parameter c and cell volume V. The shaded pink area corresponds to the biphasic domain, using a 10% phase threshold as in Fig. 7.

displacement mode with the largest amplitude remains Σ_3 [9] from 300 K down to 120 K. Its amplitude also stays constant, while the amplitudes of all the other modes stay close to zero showing that the RTM herringbone pattern of the MnO_6 distorted octahedra is preserved down to 120 K. At lower temperatures, peaks appear which cannot be indexed with only one commensurate modulation. Rather, multiple solutions consisting of several coexisting modulations along at least two cell directions are found. Consequently it is impossible to describe in detail the low-temperature crystal structure, but it is based on a complex modulation of the RTM phase, necessarily involving new distortion modes.

E. Neutron diffraction

The WISH and G4.1 NPD patterns were recorded while increasing temperature but for convenience, the structural

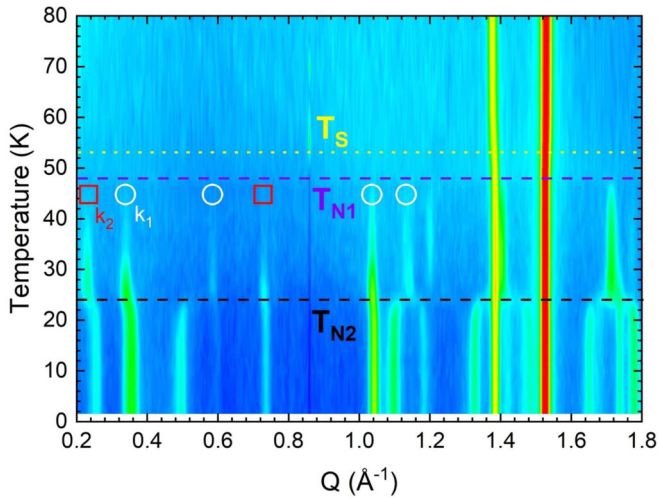

FIG. 10. Temperature evolution of the neutron-diffraction patterns (G4.1 data) in the 0.2–1.8-Å^{-1} range (patterns recorded in warming). T_S is marked in yellow, T_{N1} in purple, and T_{N2} in black. Propagation vectors (circles and squares for $\mathbf{k_1}$ and $\mathbf{k_2}$, respectively) are given for the main magnetic Bragg peaks.

evolution is described from RT to low temperatures. The evolution of the diffractograms confirms the increasing monoclinic distortion of the RTM phase down to 53 K with a broad temperature range of coexistence of RTM+LTM phases. In addition, as shown in Fig. 10, Bragg peaks of magnetic origin also appear at $T_{N1} \approx 48$ K. The Q positions of these peaks shift below $T_{N2} \approx 26$ K, in good agreement with magnetic and specific-heat measurements. Between T_{N1} and T_{N2} the magnetic Bragg peaks can be successfully indexed by two propagation vectors (Fig. 11), namely $\mathbf{k_1} = (1/2\,0\,0)$ and $\mathbf{k_2} = (0\,1/2\,0)$ using the cell parameters of the LTM phase (as given in Fig. 9), corresponding to a doubling along a and b of this LTM cell. $\mathbf{k_1}$ and $\mathbf{k_2}$ do not belong to two different phases or to decoupled sublattices, as they appear at the same temperature T_{N1} and become incommensurate concomitantly

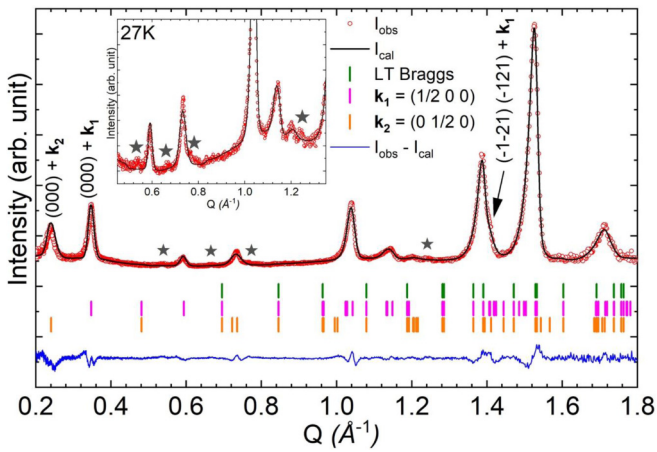

FIG. 11. Le Bail fitting of the LTM crystal structure of Mn_2TeO_6 at 27 K (WISH data), with magnetic peaks indexed with $\mathbf{k_1} = (1/2\,0\,0)$ and $\mathbf{k_2} = (0\,1/2\,0)$. Gray stars outline weak additional magnetic peaks that are enlarged in the inset.

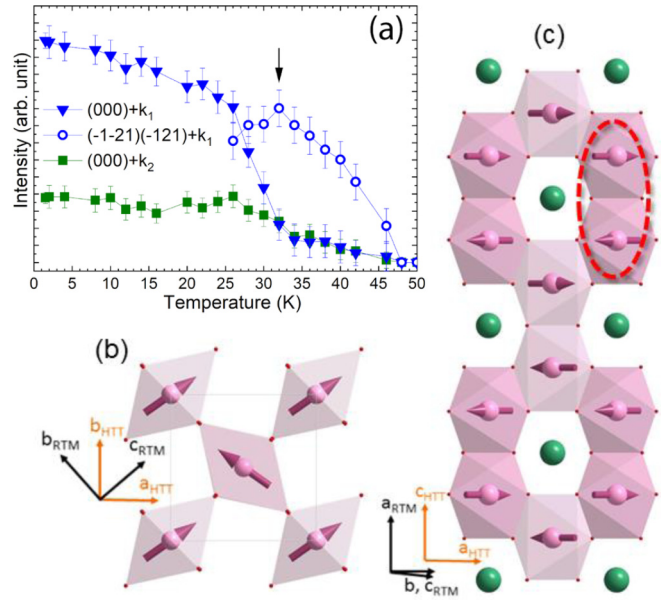

FIG. 12. (a) Temperature evolution of chosen integrated magnetic Bragg peaks (from G4.1 data). The arrow shows the maximum seen on the intensity of the $(\bar{1}\,\bar{2}1)(\bar{1}\,2\,1) + \mathbf{k_1}$ Bragg peak. (b), (c) Views of the magnetic order derived from symmetry analysis. Octahedra are drawn around Mn (pink) only (not for Te in green), the ellipse underlines a pair of edge-sharing MnO_6 octahedra, and both sets of structural axis (RTM and HTT) are given for comparison with the closely related model proposed in Ref. [8].

at T_{N2}. Below T_{N2}, no simple solution was found to describe the incommensurability of $\mathbf{k_1}$ but a possible indexation for $\mathbf{k_2}$ is $(0, 0.5 + \varepsilon'', 0)$ with $\varepsilon'' \approx 0.05$ at 1.5 K. None of these magnetic $\mathbf{k}$ vectors can index, either partially or wholly, the structural Bragg peaks appearing in the SXRPD patterns recorded below T_{N1}. More precisely, it is not possible to index even the strongest superstructure peak (seen at $\approx$1.72 Å^{-1} in the inset of Fig. 8) by either of them. Indexing this particular peak is possible with a modulation of the type (0 ¼ 0), which still fails to index all observed extra peaks, nevertheless. As a result, the Jahn-Teller distortion at the origin of the superstructure, and how it relates with spin ordering, remains unclear.

Magnetic Bragg peaks indexed with $\mathbf{k_1}$ are more intense than the ones indexed with $\mathbf{k_2}$ [Figs. 11 and 12(a)]. In addition, the temperature evolution of the intensity of magnetic peaks shows that magnetic intensity of the $(\bar{1}\,\bar{2}1)(\bar{1}\,2\,1) + \mathbf{k_1}$ peaks goes through a maximum around $\approx$33 K concomitantly with an increase of the magnetic intensities on $(0\,0\,0) + \mathbf{k_1}$ and $(0\,0\,0) + \mathbf{k_2}$. This could be linked with the very broad second-order transition discerned in this temperature range on the specific heat (Fig. 6) and susceptibility (Fig. 3) curves and could be ascribed to a spin reorientation before the incommensurate ordering at T_{N2}. There is no clear sign of subsequent magnetic transitions below 25 K on the NPD data, so that the origin of the two additional transitions on the $C_p(T)$ curve remains an open question. Moreover, very weak additional broad magnetic peaks can be seen (gray stars in Fig. 11), which are not indexed by either $\mathbf{k_1}$ or $\mathbf{k_2}$ in the commensurate

or in the incommensurate phase, suggesting an even more complex magnetic arrangement.

Even without a detailed magnetic structure, it is interesting to compare the present results with those reported by Fruchart *et al.* [8] for an unannealed sample. In their work, the magnetic ordering is described by a doubling of the tetragonal cell (equivalent to our HTT cell) along the fourfold axis (equivalent to $\mathbf{k_1}$ in the previous discussion) and corresponds to a noncollinear magnetic structure with orthogonal spins lying in the *ab* plane of the tetragonal lattice; spins within a pair of edge-sharing MnO_6 octahedra are orthogonal, and spins belonging to adjacent corner-sharing octahedra are antiparallel. This model is actually not in agreement with symmetry analysis performed on site 4*e* of $P4_2/mnm$ for $\mathbf{k} = (0\,0\,1/2)$, which can lead to a noncollinear magnetic structure with orthogonal spins, but with antiparallel spins inside the edge-sharing MnO_6 pairs, and orthogonal spins between adjacent octahedra connected by corners [Figs. 12(b) and 12(c)]. This latter model is actually more likely since the longest axes of edge-sharing octahedra are parallel, favoring parallel or antiparallel arrangements of the spins in agreement with the strong uniaxial anisotropy of Mn^{3+} [20,21]. Based on these considerations, the magnetic ordering of Mn_2TeO_6 should be seen as a complex modulation of the model proposed in Fig. 12, retaining the Mn moments in the *ab* plane of the tetragonal lattice (*bc* plane in the LTM lattice) and antiparallel spins within dimers of edge-sharing octahedra, with a modulation of either the amplitude or the orientation of the moment.

IV. DISCUSSION

The present study demonstrates that Mn_2TeO_6 exhibits structural and magnetic behaviors which are extremely complex, with six transitions, first- and second order, in C_p data below 300 K, in addition to the tetragonal to monoclinic one observed at ≈673 K (HTT to RTM) [9]. A first-order structural transition at $T_S \approx 53$ K, strongly hysteretic, occurs over a broad temperature range and is associated with a magnetic transition at $T_{N1} \approx 48$ K and a change of slope in $\varepsilon'(T)$. While NPD indicates only one other magnetic transition, at $T_{N2} \approx 26$ K, additional transitions of presumably magnetic character are identified below T_{N2}, and between T_{N1} and T_{N2}, on the C_p and $\chi(T)$ curves. Moreover, the field dependence of the magnetization differs depending on the incommensurate or commensurate character of the magnetic ordering, with in particular, a metamagnetic transition (around 4.5 T) and a negative magnetodielectric behavior (above 5 T) below T_{N2} (that is, in the incommensurate magnetic state), which do not exist for $T_{N2} < T < T_{N1}$ (commensurate magnetic state).

It is well known that orbital degrees of freedom are an important ingredient of the physics of manganites with Jahn-Teller (JT) active Mn^{3+} cations in octahedral coordination. For instance, cooperative JT distortions take place in $LaMnO_3$ up to 750 K [19,22,23]. A strong coupling between structural and magnetic transitions is also well known in $Pr_{1-x}Ca_xMnO_3$ ($x \approx 0.5$) for which the structural transition associated with orbital ordering (OO) occurs at higher temperature than the magnetic one ($T_{OO} > T_N$) [24–26] and their $\chi(T)$ curves show more clearly the structural transition than the magnetic ones. Within the crystal-field theory, the JT effect of a Mn^{3+} ($3d^4$) in octahedral symmetry and high-spin (HS) state lowers the energy of the system by lifting the orbital degeneracy between the t_{2g} and the e_g orbitals, the latter splitting into $d_{x^2-y^2}$ and d_{z^2} orbitals [27–29]. Two configurations can be obtained, either leading to an elongated octahedron (if the energy of the d_{z^2} is lower than that of the $d_{x^2-y^2}$) or to a compressed one (if d_{z^2} is the least stable orbital). Generally, the d^4 HS configuration tends to be stabilized in manganese oxides, usually with an elongation of the octahedron rather than a compression [27]. Rarely, Mn^{3+} is found in a low-spin state, with all the electrons in the t_{2g} orbitals, and therefore without JT effect [30,31].

In the HTT form of Mn_2TeO_6, MnO_6 octahedra are nearly regular, while the RTM structure shows the coexistence of two types of elongated octahedra and two types of compressed ones (Fig. 1). This unusual distortion was proposed to originate from the fact that, in each Te-Mn-Mn-Te chain, the presence of a rigid TeO_6 entity [32] on each side of the MnO_6 pair constrains it to a "local cooperative distortion" within that pair, accommodating an elongated and a compressed octahedron. Examples of compressed Mn^{3+} octahedra are rare (Ref. [33] and references therein). One of them is $CaMn_7O_{12}$, first mentioned by Bochu *et al.* [34] who wonder about their result, on the basis that only $KCuF_3$ and $KCrF_3$ are known to have apically compressed octahedra. In a recent revisiting of the $CaMn_7O_{12}$ crystal structure [35], it was shown that there is an additional structural modulation that corresponds to an incommensurate rotation of the long axes of the MnO_6 octahedra in the *xy* plane, which means that the compressed octahedra are only so in the averaged (unmodulated) structure. Coexistence of tetragonally compressed and elongated octahedra is reported in the series $Pr_{1-x}Ba_xMnO_3$ for $x = 0.35$ [36] but the difficulties encountered to detect small structural distortions with respect to the *I*4/*mcm* symmetry make other models possible. In particular, in the light of the recent discoveries on $CaMn_7O_{12}$, the existence of a structural modulation should not be excluded.

The second transition from RTM to LTM cannot be described down to the details necessary to get a proper picture of octahedral distortion. The cell volume is larger in the LTM than in the RTM phase; there is no impact on the volume at the HTT to RTM transition, but there is a substantial volume increase ($\approx +0.3\%$) between the RTM and LTM structures at ≈50 K (Fig. 9) that could be due to a release of the MnO_6 compression. In the LTM phase, there would be therefore a new orbital ordering pattern, involving the standard apically elongated octahedra in both MnO_6 octahedra of an edge-sharing pair. This in turn would allow spin ordering in the *bc* plane at lower temperature. Within such a scenario, the orbital ordering in the RTM phase could be seen as unstable or even built on a "frustrated" JT deformation of compressed MnO_6 octahedra. The JT effect would be once again the driving force behind the RTM-LTM structural transition, towards a more stable orbital ordering, based on occupied d_{z^2} orbitals confined in the *bc* plane. This would support that spins lay in the *bc* plane, in good agreement with our observations. The particular nature of this transition could also explain why it occurs over a very broad temperature range, maybe through

cooperative phenomena. The width of the biphasic domain may have an impact upon the magnetic-transition temperature if a threshold phenomenon is at play. The possibility of aging effects, reported in orbital ordered perovskite manganites [25], was tested by cycling the magnetic properties between 300 and 5 K, but no history-dependent effect was observed.

Trirutile structures with Cu^{2+} and Cr^{2+} JT active cations have been studied in the literature: $CrTa_2O_6$ [37,38], $CuTa_2O_6$ [39], and $CuSb_2O_6$ [40,41]. These compounds are also monoclinic ($P2_1/c$ or $P2_1/n$) at RT but without doubling along b, probably related to the lack of edge-sharing octahedra of JT active cations, as the sequence along the chain is $-A^{2+}B^{5+}B^{5+}A^{2+}B^{5+}B^{5+}A^{2+}$. This supports the scenario in which the key feature of Mn_2TeO_6 is its edge-sharing pairs of trivalent manganese octahedra.

V. CONCLUSION

In conclusion, this comprehensive study of inverse trirutile Mn_2TeO_6 has revealed a complex behavior, based on successive structural and magnetic transitions. Based on synchrotron x-ray diffraction, the first-order transition occurring around 53 K on the specific-heat curve corresponds to a strongly hysteretic structural transition towards a monoclinic structure of larger volume than the higher-temperature phase. Signatures of this transition also appear in the magnetization and dielectric permittivity data. The low-temperature monoclinic structure involves extra structural modulations, which remain to be understood, compared with the known RTM Mn_2TeO_6 structure. Neutron diffraction evidences a commensurate antiferromagnetic ordering below 48 K, which becomes incommensurate below 26 K. It also confirmed that structural and magnetic transitions do not occur simultaneously since T_S and T_{N1} are shifted from a few K. A scenario is proposed, based on the unusual ordering of the d_{z^2} orbitals which is found in Mn_2TeO_6 at 300 K. The existence of pairs of edge-sharing octahedra, which impose this unusual compression/elongation distortion, could be at the origin of the two Jahn-Teller induced structural transitions observed in Mn_2TeO_6 above and below RT, as well as of its complex spin ordering at low temperature.

[1] G. Bayer, J. Am. Ceram. Soc. **43**, 495 (1960).
[2] Y. Fang, L. Y. Wang, Y. Q. Song, T. Tang, D. H. Wang, and Y. W. Du, Appl. Phys. Lett. **104**, 132908 (2014).
[3] M. W. Gaultois, M. C. Kemei, J. K. Harada, and R. Seshadri, J. Appl. Phys. **117**, 014105 (2015).
[4] S. Mu and K. D. Belashchenko, J. Phys.: Condens. Matter **27**, 22203 (2015).
[5] S. D. Kaushik, B. Sahu, S. R. Mohapatra, and A. K. Singh, in *DAE Solid State Physics Symposium 2015*, edited R. Chitra, S. Bhattacharya, and N. K. Sahoo, AIP Conf. Proc. No. 1731 (AIP, New York, 2016), p. 130037.
[6] J. Wang, J. A. C. Santana, N. Wu, C. Karunakaran, J. Wang, P. A. Dowben, and C. Binek, J. Phys.: Condens. Matter **26**, 55012 (2014).
[7] F. Hund, Naturwissenschaften **58**, 323 (1971).
[8] D. Fruchart, M. C. Montmory, E. F. Bertaut, and J. C. Bernier, J. Phys. **41**, 141 (1980).
[9] N. Matsubara, F. Damay, B. Vertruyen, N. Barrier, O. I. Lebedev, P. Boullay, E. Elkaïm, P. Manuel, D. D. Khalyavin, and C. Martin, Inorg. Chem. **56**, 9742 (2017).
[10] W. Kunnmann, S. Laplaca, L. M. Corliss, J. M. Hastings, and E. Banks, J. Phys. Chem. Solids **29**, 1359 (1968).
[11] M. C. Montmory and R. Newnham, Solid State Commun. **6**, 323 (1968).
[12] M. C. Montmory, M. Belakhovsky, R. Chevalier, and R. Newnham, Solid State Commun. **6**, 317 (1968).
[13] V. Hardy, Y. Bréard, and C. Martin, J. Phys.: Condens. Matter **21**, 075403 (2009).
[14] F. Guillou, P. Courtois, L. Porcar, P. Plaindoux, D. Bourgault, and V. Hardy, J. Phys. D: Appl. Phys. **45**, 255001 (2012).
[15] F. Fauth, R. Boer, F. Gil-Ortiz, C. Popescu, O. Vallcorba, I. Peral, D. Fulla, J. Benach, and J. Juanhuix, Eur. Phys. J. Plus **130**, 160 (2015).
[16] P. J. E. M. van der Linden, M. Moretti Sala, C. Henriquet, M. Rossi, K. Ohgushi, F. Fauth, L. Simonelli, C. Marini, E. Fraga, C. Murray, J. Potter, and M. Krisch, Rev. Sci. Instrum. **87**, 115103 (2016).
[17] J. Rodriguez-Carvajal, Phys. B **192**, 55 (1993).
[18] D. Orobengoa, C. Capillas, M. I. Aroyo, and J. M. Perez-Mato, J. Appl. Crystallogr. **42**, 820 (2009).
[19] J. Rodriguez-Carvajal, M. Hennion, F. Moussa, A. H. Moudden, L. Pinsard, and A. Revcolevschi, Phys. Rev. B **57**, R3189 (1998).
[20] F. Damay, M. Poienar, C. Martin, A. Maignan, J. Rodriguez-Carvajal, G. André, and J. P. Doumerc, Phys. Rev. B **80**, 094410 (2009).
[21] N. Terada, Y. Tsuchiya, H. Kitazawa, T. Osakabe, N. Metoki, N. Igawa, and K. Ohoyama, Phys. Rev. B **84**, 064432 (2011).
[22] T. Chatterji, B. Ouladdiaf, P. Mandal, and B. Ghosh, Solid State Commun. **131**, 75 (2004).
[23] Q. Huang, A. Santoro, J. W. Lynn, R. W. Erwin, J. A. Borchers, J. L. Peng, and R. L. Greene, Phys. Rev. B **55**, 14987 (1997).
[24] Z. Jirak, S. Krupicka, Z. Simsa, M. Dlouha, and S. Vrastisla, J. Magn. Magn. Mater. **53**, 153 (1985).
[25] A. Maignan, S. Hebert, V. Hardy, C. Martin, M. Hervieu, and B. Raveau, J. Phys.: Cond. Matter **14**, 11809 (2002).
[26] C. Martin, A. Maignan, F. Damay, M. Hervieu, B. Raveau, Z. Jirak, G. André, and F. Bourée, J. Magn. Magn. Mater. **202**, 11 (1999).
[27] P. Atkins, T. Overton, J. Rourke, M. Weller, and F. Armstrong, *Shriver & Atkins Inorganic Chemistry* (Oxford University Press, Oxford, 2006).
[28] J. Goodenough, Annu. Rev. Mater. Sci. **28**, 1 (1998).
[29] M. Imada, A. Fujimori, and Y. Tokura, Rev. Mod. Phys. **70**, 1039 (1998).
[30] Z.-F. Huang, F. Du, C.-Z. Wang, D.-P. Wang, and G. Chen, Phys. Rev. B **75**, 054411 (2007).
[31] F. Aguado, F. Rodriguez, and P. Núñez, Phys. Rev. B **76**, 094417 (2007).

[32] A. G. Christy, S. J. Mills, and A. R. Kampf, Mineral. Mag. **80**, 415 (2016).

[33] S. V. Streltsov and D. I. Khomskii, Phys. Rev. B **89**, 201115(R) (2014).

[34] B. Bochu, J. Buevoz, J. Chenavas, A. Collomb, J. Joubert, and M. Marezio, Solid State Commun. **36**, 133 (1980).

[35] N. Perks, R. Johnson, C. Martin, L. Chapon, and P. Radaelli, Nat. Commun. **3**, 1277 (2012).

[36] Z. Jirak, E. Pollert, A. F. Andersen, J. C. Grenier, and P. Hagenmuller, Eur. J. Solid State Inorg. Chem. **27**, 421 (1990).

[37] M. Saes, N. P. Raju, and J. E. Greedan, J. Solid State Chem. **140**, 7 (1998).

[38] V. Guillen-Viallet, J. F. Marucco, and M. Ghysel, J. Alloys Compd. **317**, 127 (2001).

[39] A. Golubev, R. E. Dinnebier, A. Schulz, R. K. Kremer, H. Langbein, A. Senyshyn, J. M. Law, T. C. Hansen, H.-J. Koo, and M.-H. Whangbo, Inorg. Chem. **56**, 6318 (2017).

[40] D. Kasinathan, K. Koepernik, and H. Rosner, Phys. Rev. Lett. **100**, 237202 (2008).

[41] A. Nakua, H. Yun, J. Reimers, J. Greedan, and C. Stager, J. Solid State Chem. **91**, 105 (1991).